


Generalized model of MnSi-like spiral magnets

K. P. W. Hall* and S. H. Curnoe[†]

*Department of Physics and Physical Oceanography, Memorial University of Newfoundland,
St. John's, Newfoundland and Labrador, Canada A1B 3X7*

 (Received 6 May 2021; revised 12 July 2021; accepted 18 August 2021; published 7 September 2021)

A general, symmetry-allowed model of nearest-neighbor interactions for MnSi-like magnets is presented. A left-handed helical magnet phase occurs within a large parameter space of the model, which is explored via numerical simulation. The relations between microscopic features of the spiral structure and various model parameters, including an external magnetic field, are determined and show good agreement with predictions from free energy considerations. A skyrmion structure is stabilized near the boundary.

DOI: [10.1103/PhysRevB.104.094408](https://doi.org/10.1103/PhysRevB.104.094408)

I. INTRODUCTION

The B20 structure type of magnetic crystals is renowned for displaying unusual magnetic structures and for applications in a number of different fields. These diatomic materials belong to the noncentrosymmetric space group $P2_13$, which supports helimagnetic phases, arising from the absence of centrosymmetry. As such, B20 materials have been at the forefront in the study of helical magnets, where they were among the first to be experimentally observed [1–3]. In recent years there has been a resurgence of interest in these materials, MnSi in particular, due to the finding of non-Fermi-liquid behavior accompanied by partial magnetic order in the magnetic field–pressure–temperature phase diagram [4–12] and of a skyrmion crystal phase [13].

MnSi, an intermetallic compound, undergoes a phase transition at $T_c = 29$ K into a left-handed helical spin structure with wave vector \mathbf{k} oriented along one of the $\langle 111 \rangle$ directions with a wavelength of 18 nm [1–3]. Under an applied magnetic field greater than 100 mT, \mathbf{k} rotates to align with the field, and a conical spin structure is realized, where the cone angle decreases with field strength [3,14]. A field-induced ferromagnetic state appears above approximately 600 mT. The skyrmion crystal phase has been reported in “phase A,” a small pocket in the phase diagram just below T_c for small magnetic fields (≈ 100 –250 mT) [13,15]. A quantum phase transition occurs under pressure with $P_c = 14.6$ kbar accompanied by non-Fermi-liquid behavior over a wide range of temperatures [4–7,16,17].

As shown over 60 years ago, spiral magnetism arises from competing ferromagnetic (FM) and antiferromagnetic (AFM) interactions, which occur when there is more than one kind of exchange path [18] or from antisymmetric exchange interactions [known as the Dzyaloshinskii-Moriya (DM) interaction] that exist in noncentrosymmetric crystals [19,20]. Over the years these phenomenological models of MnSi have been

augmented by various additions, including gradient terms, same-site anisotropy, generalized forms of the DM interaction, and coupling to external fields, in order to quantitatively account for details of the helical structures (such as the wave number and orientation) and the nature of the phase transition to this state [21–25]. The earliest studies employed a continuum approach to the magnetization which was later extended to lattice spin models for general three-dimensional crystals [12] and finally to the actual spin lattice for MnSi-type crystals [25,26]; the latter studies describe quantitatively not only the wave number of the helical spin state but also canting of the spins and field or pressure dependence.

Recently, muon spin rotation (μ SR) studies have revealed more details of the magnetic structure in MnSi, including canting and rotation of spins within the spiral structure [27,28]. The main objective of this paper is to describe these details within a generalized model for MnSi-type crystals, constructed using only nearest-neighbor (NN) exchange interactions and single-ion anisotropy. This model will be analyzed via numerical simulations using the “effective field method” (EFM) [29].

II. THE MODEL

The magnetic ions of B20 crystals occupy the $4a$ Wyckoff position of the space group $P2_13$ (T^4 , No. 198), forming a trillium lattice as shown in Fig. 1. The four spin sites within a cubic cell are

$$\begin{aligned} \mathbf{r}_1 &= (x, x, x), \\ \mathbf{r}_2 &= \left(-x + \frac{1}{2}, -x, x + \frac{1}{2}\right), \\ \mathbf{r}_3 &= \left(-x, x + \frac{1}{2}, -x + \frac{1}{2}\right), \\ \mathbf{r}_4 &= \left(x + \frac{1}{2}, -x + \frac{1}{2}, -x\right), \end{aligned} \quad (1)$$

where the parameter $x \approx 0.138$ for Mn in MnSi. In the following, a spin located at site \mathbf{r}_i in any cubic cell will be called a $\#i$ spin.

The underlying point group of $P2_13$ is the tetrahedral group T , which has 12 symmetry elements. The corresponding

*kpwhall@mun.ca

[†]curnoe@mun.ca

operations in the space group include pure and screw rotations, but notably no inversion or reflections. None of the four sites of the $4a$ Wyckoff position are invariant under any space group operation (see Appendix for more details).

We will model magnetic interactions in B20 crystals by finding the most general form of the nearest-neighbor exchange interaction that is invariant under all space group

operations. Each site has six nearest neighbors (NNs) separated by a distance $d = a\sqrt{8x^2 - 4x + 1}/2$ which gives $d \approx 0.32a$, where $a = 4.558 \text{ \AA}$ is the lattice parameter. By considering all bilinears of the form $S_i^\alpha S_j^\beta$ (where S_i^α is the α component of the magnetic moment at site i , and j is a NN of i), it can be shown that these will combine to give 9 invariants consisting of 12 bilinears each. These are

$$\begin{aligned}
H^{xx} &= \sum_{\mathbf{n}} S_{1\mathbf{n}}^x (S_{2\mathbf{n}}^x + S_{2\mathbf{n}''}^x) + (S_{3\mathbf{n}}^x + S_{3\mathbf{n}'''}^x) S_{4\mathbf{n}'}^x + S_{1\mathbf{n}}^z (S_{3\mathbf{n}}^z + S_{3\mathbf{n}''}^z) \\
&\quad + S_{2\mathbf{n}''}^z (S_{4\mathbf{n}}^z + S_{4\mathbf{n}'}^z) + S_{1\mathbf{n}}^y (S_{4\mathbf{n}}^y + S_{4\mathbf{n}'}^y) + (S_{2\mathbf{n}}^y + S_{2\mathbf{n}'}^y) S_{3\mathbf{n}''}^y, \\
H^{yy} &= \sum_{\mathbf{n}} S_1^y S_2^y + S_3^y S_4^y + S_1^x S_3^x + S_2^x S_4^x + S_1^z S_4^z + S_2^z S_3^z, \\
H^{zz} &= \sum_{\mathbf{n}} S_1^z S_2^z + S_3^z S_4^z + S_1^y S_3^y + S_2^y S_4^y + S_1^x S_4^x + S_2^x S_3^x, \\
H_{s,a}^{xy} &= \sum_{\mathbf{n}} S_{1\mathbf{n}}^x (S_{2\mathbf{n}}^y \pm S_{2\mathbf{n}''}^y) + S_{1\mathbf{n}}^y (S_{2\mathbf{n}''}^x \pm S_{2\mathbf{n}}^x) - (S_{3\mathbf{n}}^x \pm S_{3\mathbf{n}'''}^x) S_{4\mathbf{n}'}^y - (S_{3\mathbf{n}''}^y \pm S_{3\mathbf{n}}^y) S_{4\mathbf{n}'}^x \\
&\quad + S_{1\mathbf{n}}^z (S_{3\mathbf{n}}^z \pm S_{3\mathbf{n}''}^z) + S_{1\mathbf{n}}^x (S_{3\mathbf{n}''}^z \pm S_{3\mathbf{n}}^z) - S_{2\mathbf{n}''}^z (S_{4\mathbf{n}'}^x \pm S_{4\mathbf{n}}^x) - S_{2\mathbf{n}'}^z (S_{4\mathbf{n}}^z \pm S_{4\mathbf{n}'}^z) \\
&\quad + S_{1\mathbf{n}}^y (S_{4\mathbf{n}}^z \pm S_{4\mathbf{n}'}^z) + S_{1\mathbf{n}}^z (S_{4\mathbf{n}'}^y \pm S_{4\mathbf{n}}^y) - (S_{2\mathbf{n}}^y \pm S_{2\mathbf{n}'}^y) S_{3\mathbf{n}''}^z - (S_{2\mathbf{n}'}^z \pm S_{2\mathbf{n}}^z) S_{3\mathbf{n}''}^y, \\
H_{s,a}^{yz} &= \sum_{\mathbf{n}} S_1^y S_2^z + S_3^y S_4^z + S_1^x S_3^y + S_2^x S_4^y + S_1^z S_4^x + S_2^z S_3^x, \\
H_{s,a}^{zx} &= \sum_{\mathbf{n}} S_1^z S_2^x + S_3^z S_4^x + S_1^y S_3^z + S_2^y S_4^z + S_1^x S_4^y + S_2^x S_3^y,
\end{aligned} \tag{2}$$

where \mathbf{n} is a cubic lattice vector, $\mathbf{n}' = \mathbf{n} - (1, 0, 0)$, $\mathbf{n}'' = \mathbf{n} - (0, 1, 0)$, and $\mathbf{n}''' = \mathbf{n} - (0, 0, 1)$. The terms in H_{yy} and H_{zz} have been abbreviated; their full forms are analogous to those in H_{xx} . Likewise, the full forms of the terms in $H_{s,a}^{yz}$ and $H_{s,a}^{zx}$ can be constructed similarly to $H_{s,a}^{xy}$. We also include the Zeeman term

$$H_Z = -\mathbf{H} \cdot \sum_{\mathbf{n},i} \mathbf{S}_{\mathbf{n},i}, \tag{3}$$

where \mathbf{H} is an applied field. Lastly, we consider same-site anisotropy terms at second and fourth order:

$$\begin{aligned}
H_2 &= \sum_{\mathbf{n},i} \mathbf{S}_{\mathbf{n},i}^x \mathbf{S}_{\mathbf{n},i}^y + \mathbf{S}_{\mathbf{n},i}^x \mathbf{S}_{\mathbf{n},i}^z + \mathbf{S}_{\mathbf{n},i}^y \mathbf{S}_{\mathbf{n},i}^z, \\
H_4 &= \sum_{\mathbf{n},i} |\mathbf{S}_{\mathbf{n},i}|^4.
\end{aligned} \tag{4}$$

Computational studies typically use fewer parameters by taking specific combinations of the terms given in (2). For example, the NN Heisenberg exchange interaction is

$$\sum_{\langle i,j \rangle} \mathbf{S}_i \cdot \mathbf{S}_j = H^{xx} + H^{yy} + H^{zz}. \tag{5}$$

The NN Dzyaloshinskii-Moriya (DM) interaction is

$$\sum_{\langle i,j \rangle} \mathbf{D}_{ij} \cdot (\mathbf{S}_i \times \mathbf{S}_j), \tag{6}$$

where the DM vectors \mathbf{D}_{ij} are constrained by the symmetry of the lattice. The DM interaction corresponds to the three anti-symmetric (subscript a) terms in (2); in fact, comparison with these terms yields the minimal constraints on the DM vectors. For example, examining the terms in H_a^{xy} yields $D_{1\mathbf{n}2\mathbf{n}}^z = -D_{1\mathbf{n}2\mathbf{n}''}^z = -D_{3\mathbf{n}4\mathbf{n}'}^z = D_{3\mathbf{n}''4\mathbf{n}'}^z = -D_{1\mathbf{n}3\mathbf{n}}^z = D_{1\mathbf{n}3\mathbf{n}''}^z \dots$. The DM vectors are often further constrained by taking the DM term to be $H_a^{xy} + H_a^{yz} + H_a^{zx}$. The symmetric terms $H_s^{\alpha\beta}$ are usually omitted altogether.

In our simulations, we consider a free energy constructed using all nine of the exchange terms (2) and the two same-site anisotropy terms (4), for a total of 11 independent interaction constants, as well as the Zeeman term (3):

$$\begin{aligned}
F &= \mathcal{J}^{xx} H^{xx} + \mathcal{J}^{yy} H^{yy} + \mathcal{J}^{zz} H^{zz} + \mathcal{J}_s^{xy} H_s^{xy} + \mathcal{J}_a^{xy} H_a^{xy} \\
&\quad + \dots + \mathcal{J}_2 H_2 + \mathcal{J}_4 H_4 + H_Z.
\end{aligned} \tag{7}$$

III. MAGNETIC ORDER PARAMETERS

The helical magnet phase of MnSi is marked by the appearance of a left-handed spiral oriented along one of the four equivalent $\langle 111 \rangle$ directions. From here on, we will assume that the helices are oriented in the particular direction $[111]$. Perpendicular to $[111]$ are alternating planes of #1 spins and of #2, 3, and 4 spins, which we label 1 and 2-3-4, respectively (see Fig. 1). Moving along the $[111]$ direction, the distance between a 1-plane and the following 2-3-4-plane is

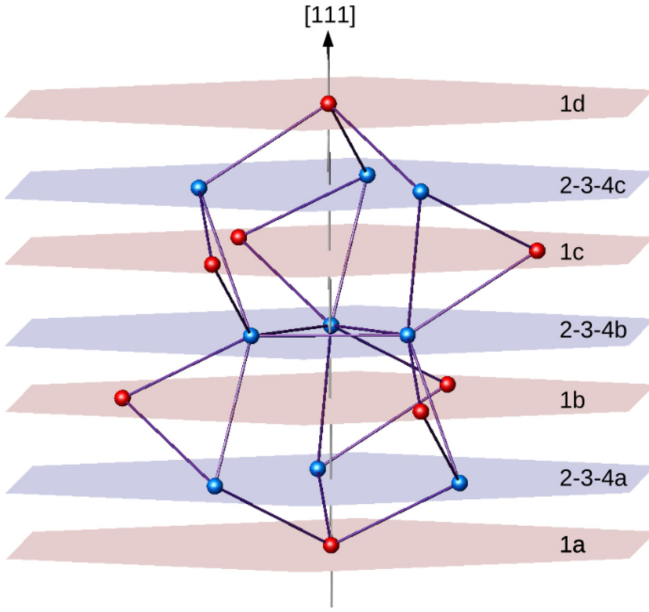


FIG. 1. The crystal structure of $P2_13$ crystals with $x = 0.138$ —the lattice parameter associated with MnSi. The spins form triangular lattices in planes perpendicular to the cubic diagonals; for the $[111]$ direction considered here, there are alternating layers of #1 spins (red) and #2, 3, and 4 spins (blue). The distance from layer 1a to 1d is $\sqrt{3}a$, one cubic diagonal along the $[111]$ direction. Nearest neighbors are connected by lines.

$(1 - 4x)a/\sqrt{3} = 0.259a$, and the distance between a 2-3-4-plane and the next 1-plane is $4xa/\sqrt{3} = 0.319a$.

In order to classify magnetic structures, we define magnetic order parameters associated with $\mathbf{k} \parallel [111]$. The little group of this wave vector is C_3 , a subgroup of the crystallographic point group T . The three representations that belong to $\mathbf{k} \parallel [111]$, labeled F_1 , F_2 , and F_3 , are derived from the three representations of C_3 . All three are one dimensional; F_2 and F_3 are related by time reversal.

The 12-dimensional basis of 4 spins within a unit cell and 3 spatial dimensions generates a (reducible) representation belonging to $\mathbf{k} \parallel [111]$, $4F_1 \oplus 4F_2 \oplus 4F_3$; that is, there are four copies of each irreducible representation. The basis is

$$F_1^{(1)} = S_{1\mathbf{k}}^x + S_{1\mathbf{k}}^y + S_{1\mathbf{k}}^z, \quad (8)$$

$$F_2^{(1)} = S_{1\mathbf{k}}^x + \varepsilon S_{1\mathbf{k}}^y + \varepsilon^2 S_{1\mathbf{k}}^z, \quad (9)$$

$$F_3^{(1)} = S_{1\mathbf{k}}^x + \varepsilon^2 S_{1\mathbf{k}}^y + \varepsilon S_{1\mathbf{k}}^z, \quad (10)$$

$$F_1^{(2)} = S_{2\mathbf{k}}^x + S_{4\mathbf{k}}^y + S_{3\mathbf{k}}^z, \quad (11)$$

$$F_2^{(2)} = S_{2\mathbf{k}}^x + \varepsilon S_{4\mathbf{k}}^y + \varepsilon^2 S_{3\mathbf{k}}^z, \quad (12)$$

$$F_3^{(2)} = S_{2\mathbf{k}}^x + \varepsilon^2 S_{4\mathbf{k}}^y + \varepsilon S_{3\mathbf{k}}^z, \quad (13)$$

$$F_1^{(3)} = S_{2\mathbf{k}}^y + S_{4\mathbf{k}}^z + S_{3\mathbf{k}}^x, \quad (14)$$

$$F_2^{(3)} = S_{2\mathbf{k}}^y + \varepsilon S_{4\mathbf{k}}^z + \varepsilon^2 S_{3\mathbf{k}}^x, \quad (15)$$

$$F_3^{(3)} = S_{2\mathbf{k}}^y + \varepsilon^2 S_{4\mathbf{k}}^z + \varepsilon S_{3\mathbf{k}}^x, \quad (16)$$

$$F_1^{(4)} = S_{2\mathbf{k}}^z + S_{4\mathbf{k}}^x + S_{3\mathbf{k}}^y, \quad (17)$$

$$F_2^{(4)} = S_{2\mathbf{k}}^z + \varepsilon S_{4\mathbf{k}}^x + \varepsilon^2 S_{3\mathbf{k}}^y, \quad (18)$$

$$F_3^{(4)} = S_{2\mathbf{k}}^z + \varepsilon^2 S_{4\mathbf{k}}^x + \varepsilon S_{3\mathbf{k}}^y, \quad (19)$$

where $\varepsilon = \exp 4\pi i/3 = -\frac{1}{2} - i\frac{\sqrt{3}}{2}$ and $\varepsilon^2 = \varepsilon^*$. $S_{i\mathbf{k}}^\alpha$ are the Fourier transforms of the spins,

$$S_{i\mathbf{k}}^\alpha = \frac{1}{N^{1/2}} \sum_{\mathbf{n}} \exp(-i\mathbf{k} \cdot \mathbf{r}_{i\mathbf{n}}) S_{i\mathbf{n}}^\alpha, \quad (20)$$

where $\mathbf{r}_{\mathbf{n}}$ is the \mathbf{n} th lattice vector and N is the total number of cells. The physical spins are $S_{i\mathbf{n}}^\alpha$; that is,

$$S_{i\mathbf{k}}^\alpha = \frac{1}{N^{1/2}} \sum_{\mathbf{k}} S_{i\mathbf{k}}^\alpha \exp(i\mathbf{k} \cdot \mathbf{r}_{i\mathbf{n}}). \quad (21)$$

There is no sum over wave number in this expression when \mathbf{k} is the only wave vector present in the structure.

The helical magnet phase of MnSi is marked by the appearance of a left-handed spiral, which corresponds to an order parameter that transforms as F_3 , i.e., one or more of the $F_3^{(i)}$ are nonzero while $F_2^{(i)} = 0$. That is, the spins precess in a clockwise direction with respect to the $[111]$ direction. Since F_1 is compatible with F_3 (in the sense that no additional symmetries are broken by F_1), there is no requirement that $F_1^{(i)}$ be vanishing.

The spin arrangements associated with a F_3 order parameter are in general quite complicated; here, we make some simplifying assumptions based on experimental observations. First, we assume that the magnitude of individual spins is fixed. If $F_3^{(1)}$ is present and not $F_2^{(1)}$, then this constraint forces $F_1^{(1)}$ to be absent in order for spin #1 to have fixed length. This means that spin #1 must be perpendicular to the $[111]$ axis, i.e., no canting of this spin toward $[111]$ is expected, as seen in experiment.

If we also assume that spins #2, 3, and 4 have the same magnitudes, then the relative magnitudes of the various order parameters will be constrained, but there is no requirement that $F_1^{(i)}$ must vanish if $F_3^{(i)}$ is present and not $F_2^{(i)}$ for $i = 2, 3, 4$. However, in experiments it is observed that spins #2, 3, and 4 lie perpendicular to \mathbf{k} in ferromagnetic arrangements within each 2-3-4-plane [27]. In this arrangement, if $F_2^{(i)}$ vanishes, then $F_1^{(i)}$ also vanishes and the components of $F_3^{(i)}$ are related by $F_3^{(2)} = \varepsilon^2 F_3^{(3)} = \varepsilon F_3^{(4)}$.

Even with all these constraints imposed, there remains a free parameter accessible by experiment: the relative orientation of spins in a 1-plane with respect to the nearest 2-3-4-plane [27]. The spins precess in a left-handed sense for a distance d along the $[111]$ direction by an angle kd rad, where $k = 0.35 \text{ nm}^{-1}$. The precession angle between planes of the same type is therefore $ka/\sqrt{3}$ rad or 5.28° . According to this simple picture, the precession angle between a 2-3-4-plane and the next 1-plane would be 2.913° ; however, this angle is measured to be only 0.86° [27]. The phase difference $\phi = -2.04^\circ$ (-0.0356 rad) can be considered as a model-dependent parameter. The angle ϕ is illustrated in Fig. 2.

The only constraint we enforce in our numerical simulations is that all four spins have constant, equal magnitudes.

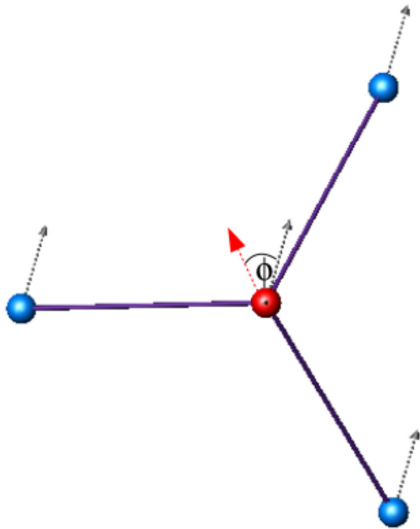


FIG. 2. Illustration of the angle ϕ . Layers 2-3-4c and 1d from Fig. 1 are viewed from above the $[111]$ axis. The gray arrows on the 2-3-4 sites (blue) are for reference. The gray arrow on the red site indicates the orientation of the spin which would be expected considering only the helical wave vector and the distance between layers, i.e., the gray arrow on site #1 (red) is rotated by an angle 2.913° with respect to the gray arrows on sites #2, 3, and 4. The red arrow shows how the angle ϕ is defined: It is the deviation of the actual orientation of spin #1 from the expected orientation. This angle has been observed to be $\phi \approx -2^\circ$ (note that it is *negative*, while in the figure a much larger, *positive* $\phi \approx 35^\circ$ is shown for clarity).

We find that spins in the 2-3-4-planes do not always lie perpendicular to \mathbf{k} . Generally, they precess within different planes, which gives rise to another model-dependent parameter, the angle $\gamma^{(2)}$, which we define as the angle between the $[111]$ plane and the actual plane of the spins, which is different for each of spins #2, 3, and 4 (i.e., they are not ferromagnetically aligned within each 2-3-4-plane). In fact, the plane of each spin S_i will cant toward τ_i , where

$$\begin{aligned}\tau_2 &= [\bar{1}\bar{1}\bar{1}], \\ \tau_3 &= [\bar{1}\bar{1}\bar{1}], \\ \tau_4 &= [1\bar{1}\bar{1}],\end{aligned}\quad (22)$$

as illustrated in Fig. 3.

We also define the angle $\gamma^{(1)}$ which measures the canting of spin #1 away from the $[111]$ plane. The angles $\gamma^{(1)}$ and $\gamma^{(2)}$ have not been measured in experiment, but they have been predicted by analysis of the free energy [26]. In our simulations, $\gamma^{(1)}$ and $\gamma^{(2)}$ are measured as the average canting away from the $[111]$ plane.

IV. RESULTS

The EFM is a computational method used for determining the spin configuration of a system as $T \rightarrow 0$ by finding local minima of the free energy in classical and semiclassical systems with pairwise interactions. The method uses an iterative algorithm which, in each step, scans all spins in a random

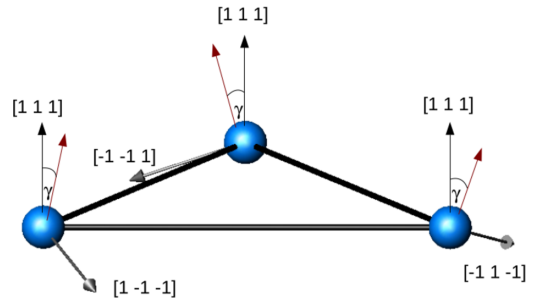


FIG. 3. Illustration of the angle $\gamma^{(2)}$ (shown as γ in the figure). Layer 2-3-4b of Fig. 1 is shown. When $\gamma^{(2)}$ is zero, each spin lies in a plane that is normal to $[111]$ (shown as black arrows). The actual planes of the spins are perpendicular to the red arrows and are tilted by an angle $\gamma^{(2)}$ towards the planes perpendicular to τ_i (gray arrows).

order. For each spin site, a *local field* is calculated,

$$H_i^\alpha = - \sum_{j,\beta} \mathcal{J}_{i,j}^{\alpha,\beta} S_j^\beta, \quad (23)$$

where S_j are the spins with which S_i interacts and $\mathcal{J}_{i,j}^{\alpha,\beta}$ is the total of all interaction constants for S_i^α and S_j^β . The spin located at i is then reoriented, either fully or partially, in the direction of this field. This process is repeated many times until a local minimum is found. Since the algorithm has no process by which a given spin can increase its interaction energy, it is likely that the final lattice configuration will not be the global minimum. This is remedied by running the algorithm a large number of times with randomly generated starting configurations. From this set of simulations, only those which produce the lowest energy are selected.

Since we are primarily interested in modeling the helical phase, we begin by considering a set of interaction constants which yields such a configuration, and then we vary those parameters in order to discern their individual effect on the magnetic structures. For each simulation, we measure the wave number k , the phase difference ϕ , the out-of-plane canting angle γ (with respect to the $[111]$ plane), and the relative size of the magnetic order parameters $|F_i^{(j)}|$. All simulations were performed on a system with $23 \times 23 \times 23$ cells (large enough to contain one full wavelength of the helix) with 48 668 spins in total. In order to find an incommensurate k , periodic boundary conditions were *not* imposed.

A. Reduced model

We begin by examining a model with only two parameters, J and D , defined by

$$J = \mathcal{J}^{xx} = \mathcal{J}^{yy} = \mathcal{J}^{zz}, \quad (24)$$

$$D = \mathcal{J}_a^{xy} = \mathcal{J}_a^{yz} = \mathcal{J}_a^{zx}, \quad (25)$$

corresponding to the Heisenberg exchange interaction and a simplified DM interaction where all components of the DM vector are $\pm D$. In all simulations, we used $\mathcal{J}_2 = -J/2$, $\mathcal{J}_4 = J/2$ with all other constants being zero. The sign of D is negative, yielding a left-handed spiral.

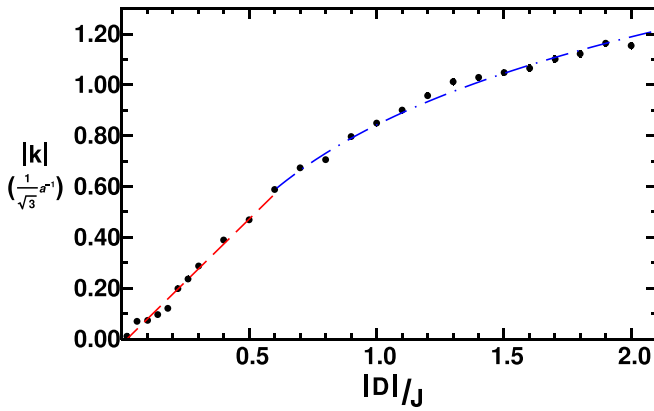


FIG. 4. Average wave vector k as a function of $|D|/J$. For $|D|/J < 0.6$ a linear fit is shown (red; dashed curve). For $|D|/J > 0.6$ a logarithmic fit is shown (blue; dot-dashed curve).

The wavelength was measured using the average rotation between unit cells along $[111]$. As shown in Fig. 4, for small $|D|$, we find a linear relationship between wave number k and $|D|$, as predicted from free energy considerations [21]. Nonlinear deviations occur for $|D|/J \gtrsim 0.6$. The measured wavelength is $\lambda = 18 \text{ nm} = 22.8\sqrt{3}a$, which is 22.8 unit cells along the $\langle 111 \rangle$ direction. The corresponding wave number is $k = 0.276/(\sqrt{3}a)$, which occurs for $|D|/J \approx 0.3$.

Figure 5 shows the phase difference ϕ (defined at the end of Sec. III) as a function of $|D|/J$. ϕ is the average of phase differences measured between a 1-plane and a 2-3-4-plane. There is a linear relation between ϕ and $|D|/J$, as predicted from free energy considerations [26]. The value of $|D|/J \approx 0.3$ yields a phase difference $\phi \approx -0.07 \text{ rad}$, which is approximately twice as large as the measured value [27].

Figure 6 shows the angles $\gamma^{(1)}$ and $\gamma^{(2)}$ (defined at the end of Sec. III) as a function of $|D|/J$. In our simulations, $\gamma^{(2)}$ is measured by assuming that all spins associated with a given position rotate within the same plane and measuring the angle between the $[111]$ axis and the normal vector of this plane. $\gamma^{(1)}$ is the average of angles measured for each spin. The canting of spins in a 1-plane ($\gamma^{(1)}$) is always small, which correlates with a vanishing F_1 order parameter, as shown in

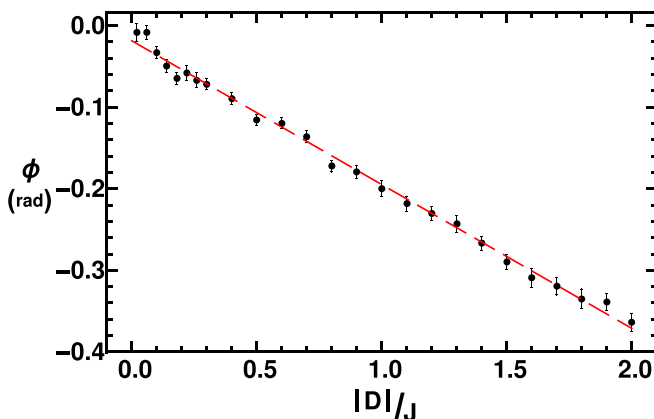


FIG. 5. Phase difference ϕ as a function of $|D|/J$. A linear fit is shown.

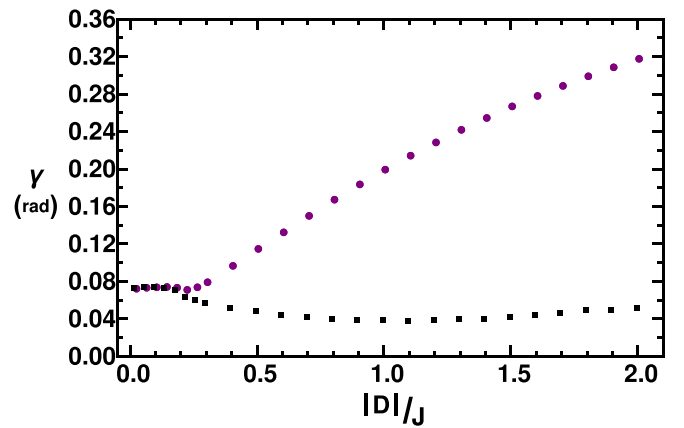


FIG. 6. The average out-of-plane angle $\gamma^{(1)}$ for the 1-plane (black squares) and $\gamma^{(2)}$ for the 2-3-4-plane (purple circles). In the 2-3-4-planes, the spins of the same # in a given layer have the same orientation.

Fig. 7. However, the canting of the spins in a 2-3-4-plane increases with $|D|/J$, as expected from the free energy considerations [26]. Using the value $|D|/J \approx 0.3$ (determined from our measurements of \mathbf{k}), we estimate that $\gamma \approx 4.6^\circ$ for the 2-3-4-plane in MnSi.

Figure 7 shows magnetic order parameters, calculated by taking the absolute value of the functions $F_i^{(j)}$ defined in Eqs. (8)–(19), as a function of $|D|/J$. The summations are calculated using the assumption that $\mathbf{k} \parallel [111]$, with the magnitude of k determined by our simulations (see Fig. 4).

In order to make it easier to compare the relative sizes of the order parameters, the plots in Fig. 7 have been normalized at each value of $|D|/J$ such that the highest value is 1. In fact, the scale of each plot decreases with $|D|/J$, indicating a transfer of weight to other values of k with increasing $|D|/J$. This is most likely due to the finite size and nonperiodic boundary conditions of our simulation.

Figure 7 shows that at larger wavelengths (small $|D|/J$) there is a mixture of F_2 and F_3 order parameters, corresponding to right-handed and left-handed structures, but the

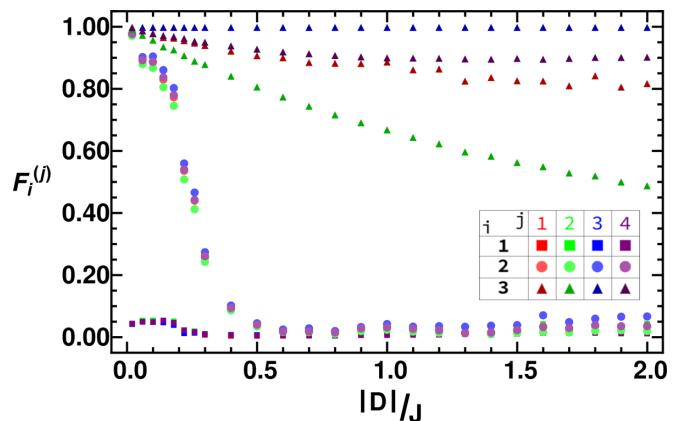


FIG. 7. The averaged magnetic order parameters derived from Eqs. (8)–(19) as a function of $|D|/J$. The plots are normalized such that the maximum size of any order parameter at each value of $|D|/J$ is always 1.

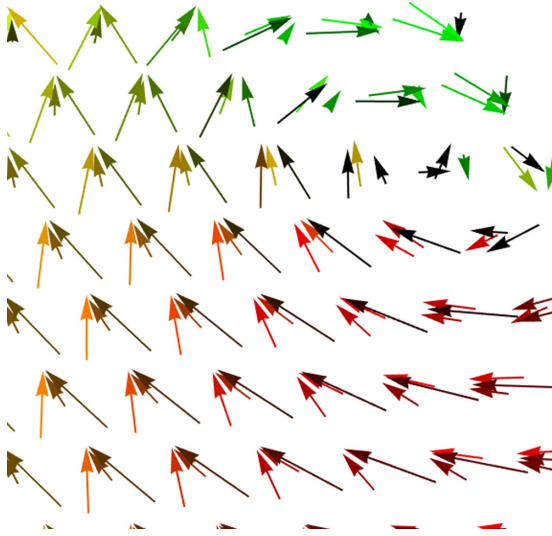


FIG. 8. Example of a skyrmion spin configuration for $|D|/J = 2.00$. The hue of the arrow varies with the angle within the [111] plane, while the brightness represents the magnitude of the out-of-plane angle (darker arrows have a larger out-of-plane angle).

right-handed part quickly decreases with respect to the left-handed part as the wavelength decreases. At $|D|/J \approx 0.3$, the left-handed component is five times larger than the right-handed component, and all four parts of the left-handed order parameter are present, but not equal.

There is a slight increase in F_1 order parameters with larger values of $|D|/J$. This coincides with the appearance of isolated Bloch-type skyrmions in our simulations around $|D|/J \approx 1.6$. An example is shown in Fig. 8. When present, skyrmions always appear near the simulation boundary as a small tunnel approximately oriented along the $\mathbf{k} \parallel [111]$ direction with a length of only a few layers.

B. Individual model terms

In this section, we examine the effects of each independent interaction constant. As the starting point, we use a set of parameters which yield a left-handed helix: $J = 1$, $D = -0.5$, $\mathcal{J}_2 = -0.5$, $\mathcal{J}_4 = 0.5$, with all other constants vanishing. We vary the nine interaction constants around this point in order to examine the dependence of k , ϕ , and γ on these parameters. In the following, we present those results where the dependence on individual parameters is most pronounced. Complete details of all of the simulations may be found in Ref. [30].

Figure 9 shows the dependence of the out-of-plane angles $\gamma^{(1)}$ and $\gamma^{(2)}$ on the three symmetric exchange parameters \mathcal{J}^{xx} , \mathcal{J}^{yy} , and \mathcal{J}^{zz} . For both angles we note the strongest dependence on \mathcal{J}^{zz} , while \mathcal{J}^{xx} yields nearly constant results. For $\gamma^{(1)}$, the slopes of the lines for \mathcal{J}^{zz} and \mathcal{J}^{yy} have the opposite sign.

Figure 10 shows the dependence of k , ϕ , and $\gamma^{(2)}$ on the antisymmetric exchange constants \mathcal{J}_a^{ij} . The wave-number results are similar to what is shown in Fig. 4, except for the variation of \mathcal{J}_a^{zx} , which has a linear dependence of the opposite sign. The plots for ϕ and $\gamma_2^{(2)}$ also display linear dependence similar to what is shown in Figs. 2 and 3, except

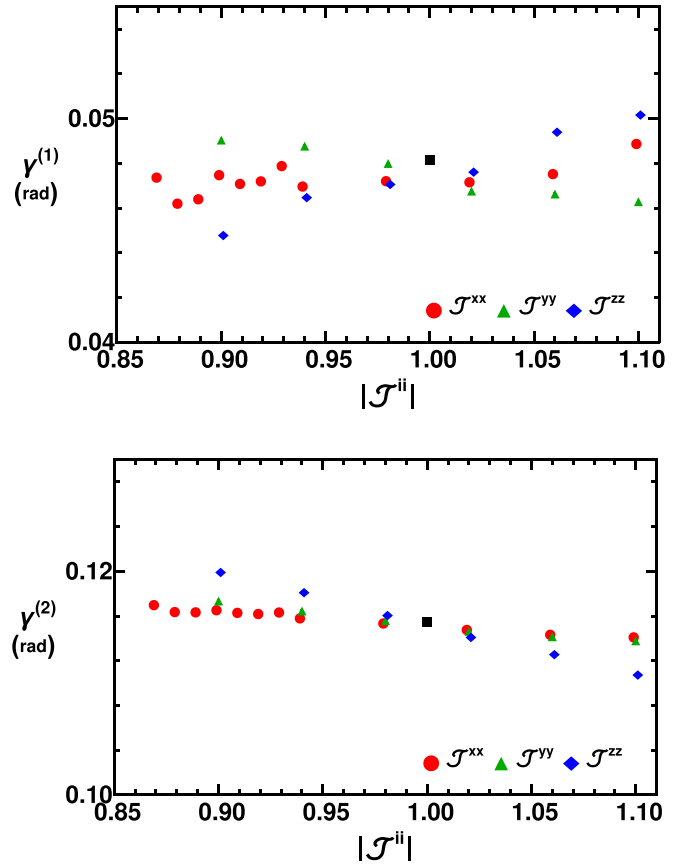


FIG. 9. The out-of-plane angles $\gamma^{(1)}$ and $\gamma^{(2)}$ as a function of individual symmetric (Heisenberg-like) coupling constants. The black square represents the $|D| = 0.50$ result.

for the parameter \mathcal{J}_a^{xy} , where the dependence is almost flat. It is clear from the plots that all three measurable quantities are sensitive to the tuning of the three antisymmetric exchange constants, especially the phase difference ϕ , which varies by as much as 50% in the (limited) range shown in the plot.

The independent variation of the antisymmetric interaction constants was analyzed by Chizhikov and Dmitrienko [26], who used the notation $(D_x, D_y, D_z) \equiv (\mathcal{J}_a^{zx}, \mathcal{J}_a^{xy}, \mathcal{J}_a^{yz})$. They found

$$k = \frac{2(D_x - 2D_y - D_z)}{3J}, \quad (26)$$

$$\phi \propto \frac{D_x + D_z}{J}, \quad (27)$$

$$\gamma \propto -\frac{(D_x + D_z)}{J}, \quad (28)$$

in rough agreement with the results shown in Fig. 10. In particular, these results predict the flatness of the plots for ϕ and $\gamma^{(2)}$ with respect to the parameter \mathcal{J}_a^{xy} , as well as the relative sizes and signs of the slopes of the plots for k .

It is worth noting that, although it begins with a four-parameter model, Ref. [26] finds the other five independent nearest-neighbor interaction terms as renormalized corrections to the free energy. First there is a small correction to the Heisenberg interaction constant $-J \rightarrow -J + \frac{D^2}{12J}$ with separate, additional contributions to each

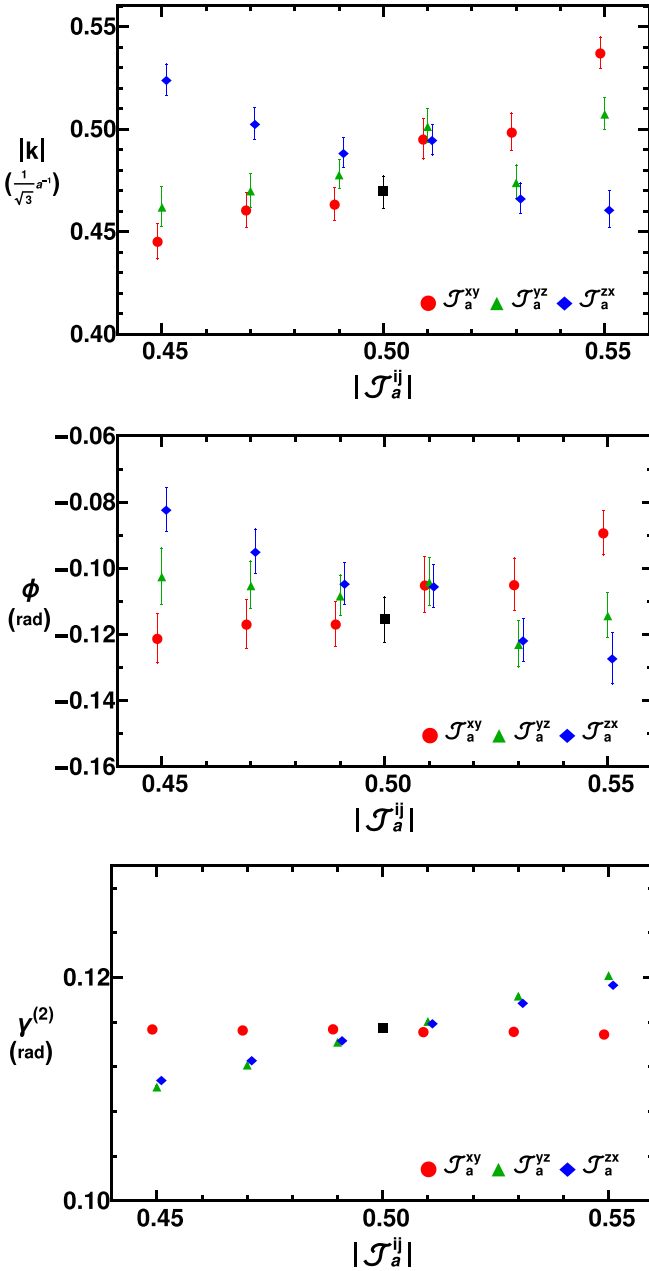


FIG. 10. Wave number k , angle ϕ , and out-of-plane angle $\gamma^{(2)}$ as functions of the antisymmetric coupling constants \mathcal{J}_a^{ij} . The black square is the $|D| = 0.50$ result. In the bottom plot the error bars are too small to be seen.

of the components in $(\mathcal{J}^{xx}, \mathcal{J}^{yy}, \mathcal{J}^{zz})$: $\frac{-1}{6J}(2D_z^2 - D_x^2 - D_y^2, 2D_x^2 - D_y^2 - D_z^2, 2D_y^2 - D_x^2 - D_z^2)$. The other symmetric interaction constants also appear as $(\mathcal{J}_s^{yz}, \mathcal{J}_s^{zx}, \mathcal{J}_s^{xy}) \equiv \frac{-1}{2J}(D_x D_y, D_y D_z, D_z D_x)$. However, the analysis of the k , ϕ , and γ in Ref. [26] does not consider these contributions.

C. Applied field

We also performed numerical simulations of the model under an applied magnetic field, where the field is scaled according to Eq. (3). As in Sec. IV B, the model is set to the parameters $J = 1$, $D = -0.5$, $\mathcal{J}_2 = -0.5$, $\mathcal{J}_4 = 0.5$, with all other constants vanishing. Figure 11 shows the out-of-plane

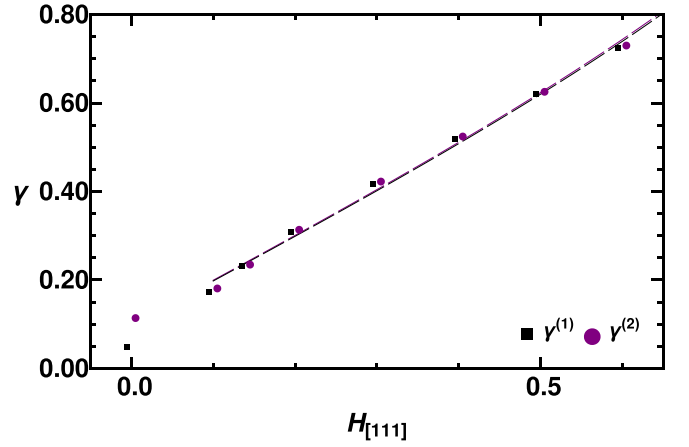


FIG. 11. The out-of-plane canting of individual sublattices as a function of applied field. The lines are fits to the function $c + \arcsin(aH)$.

canting of the spins as a function of an applied field in the [111] direction. As expected, with increasing field, canting toward the field direction increases as $\arcsin(H)$, and there is little difference between $\gamma^{(1)}$ and $\gamma^{(2)}$. Extrapolating the fit, complete alignment of the moments with the field occurs when $H \sim 1$.

Figure 12 shows how the components of the order parameter evolve as a function of an applied field in the [111] direction. The F_i components increase with increasing field, until they become the dominant contribution, in rough correspondence with the out-of-plane canting shown in Fig. 11.

V. DISCUSSION AND CONCLUSIONS

The computational results of the simplified two-parameter model discussed in Sec. IV A provide a qualitative description of the helical magnet phase of MnSi but fail to describe it in detail: The measured values of k and ϕ cannot be consistently explained within a two-parameter model of symmetric and antisymmetric interactions. Our numerical simulations using the full model, presented in Sec. IV B, demonstrate that an

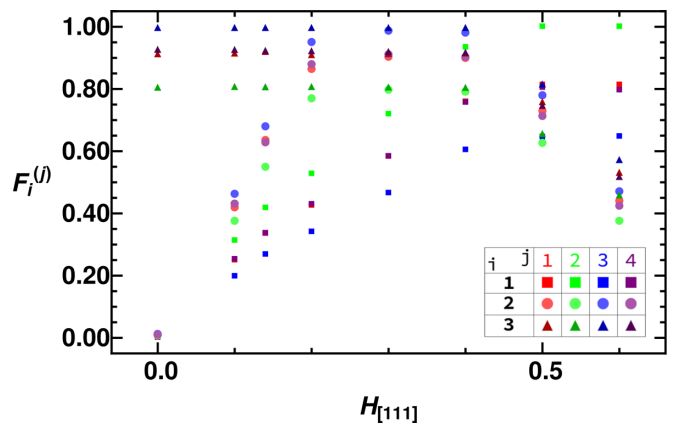


FIG. 12. Magnetic order parameters vs applied field in the [111] direction. The magnitudes are normalized within a single value of H such that the maximum is always 1.0.

TABLE I. The 12 point-group symmetry operations of the space group $P2_13$. The action of each operation on the magnetic ion positions is given in the third, fourth, fifth, and sixth columns. The three-digit subscript is the translation with respect to a reference unit cell at 000. The seventh column lists the coordinate transformations.

Operation No.	Symmetry operation	S_{1000}	S_{2000}	S_{3000}	S_{4000}	(x, y, z)
(1)	1	S_{1000}	S_{2000}	S_{3000}	S_{4000}	(x, y, z)
(2)	$2(0, 0, \frac{1}{2}) \quad \frac{1}{4}, 0, z$	S_{2000}	S_{1001}	S_{4011}	S_{3010}	(\bar{x}, \bar{y}, z)
(3)	$2(0, \frac{1}{2}, 0) \quad 0, y, \frac{1}{4}$	S_{3000}	S_{4100}	S_{1010}	S_{2110}	(\bar{x}, y, \bar{z})
(4)	$2(\frac{1}{2}, 0, 0) \quad x, \frac{1}{4}, 0$	S_{4000}	S_{3101}	S_{2001}	S_{1100}	(x, \bar{y}, \bar{z})
(5)	$3^+ \quad x, x, x$	S_{1000}	S_{4000}	S_{2000}	S_{3000}	(z, x, y)
(6)	$3^+ \quad \bar{x} + \frac{1}{2}, x, \bar{x}$	S_{4000}	S_{1100}	S_{3101}	S_{2001}	(z, \bar{x}, \bar{y})
(7)	$3^+ \quad x + \frac{1}{2}, \bar{x} - \frac{1}{2}, \bar{x}$	S_{2000}	S_{3010}	S_{1001}	S_{4011}	(\bar{z}, \bar{x}, y)
(8)	$3^+ \quad \bar{x}, \bar{x} + \frac{1}{2}, x$	S_{3000}	S_{2110}	S_{4100}	S_{1010}	(\bar{z}, x, \bar{y})
(9)	$3^- \quad x, x, x$	S_{1000}	S_{3000}	S_{4000}	S_{2000}	(y, z, x)
(10)	$3^- \quad (-\frac{1}{3}, \frac{1}{3}, \frac{1}{3}) \quad x + \frac{1}{6}, \bar{x} + \frac{1}{6}, \bar{x}$	S_{3000}	S_{1010}	S_{2110}	S_{4100}	(\bar{y}, z, \bar{x})
(11)	$3^- \quad (\frac{1}{3}, \frac{1}{3}, -\frac{1}{3}) \quad \bar{x} + \frac{1}{3}, \bar{x} + \frac{1}{6}, x$	S_{4000}	S_{2100}	S_{1100}	S_{3101}	(y, \bar{z}, \bar{x})
(12)	$3^- \quad (\frac{1}{3}, -\frac{1}{3}, \frac{1}{3}) \quad \bar{x} - \frac{1}{6}, x + \frac{1}{3}, \bar{x}$	S_{2000}	S_{4011}	S_{3010}	S_{1001}	(\bar{y}, \bar{z}, x)

appropriate tuning of the parameters of the more general model could reproduce those experimentally measured values. Also, in our simulations, we have measured other features of the spin configuration in the helical phase that are potentially experimentally accessible—the out-of-plane angles $\gamma^{(1)}$ and $\gamma^{(2)}$. Our results are in good agreement with the free energy analysis of Ref. [26]. Furthermore, an additional measurement, the canting of individual spins towards their τ_i axes [Eq. (21)], could also be obtained from our results.

We have also shown—at least within the limits of our finite-sized simulation—the extent to which the helical phase is contained within a single kind of order parameter (the F_3 order parameter), and the relative weight of the four separate contributions to F_3 . Their evolution under an applied field was also presented. These details can provide a different point of comparison for measurements on the helical phase.

To summarize, we have considered a generalized, symmetry-allowed model with 11 free parameters—9 nearest-neighbor interaction constants and 2 same-site anisotropy constants—to describe the helical magnet phase in MnSi-like crystals. Experimental observations greatly constrain the

parameter space of this model, as shown in the earliest theoretical studies, which derived the relationship between symmetric and antisymmetric (DM) interaction constants and the spiral wavelength. Recent experiments have uncovered details concerning the orientation of individual magnetic moments in the magnetic spirals; those findings can be explained by the more detailed model we have considered here.

ACKNOWLEDGMENTS

This work was supported by the Natural Sciences and Engineering Research Council of Canada (RGPIN-05615-2020).

APPENDIX: CRYSTAL SYMMETRY

The nine nearest-neighbor interaction terms of the free energy are invariant under the symmetry operations (translations and rotations) of the space group $P2_13$. The actions of the rotations on the magnetic ions at positions #1–4 are listed in Table I.

- | | |
|---|--|
| [1] H. J. Williams, J. H. Wernick, R. C. Sherwood, and G. K. Wertheim, <i>J. Appl. Phys. (Melville, NY)</i> 37 , 1256 (1966). | [8] S. Tewari, D. Belitz, and T. R. Kirkpatrick, <i>Phys. Rev. Lett.</i> 96 , 047207 (2006). |
| [2] L. Lundgren, O. Beckman, V. Attia, S. P. Bhattacharjee, and M. Richardson, <i>Phys. Scr.</i> 1 , 69 (1970). | [9] B. Binz, A. Vishwanath, and V. Aji, <i>Phys. Rev. Lett.</i> 96 , 207202 (2006). |
| [3] Y. Ishikawa, K. Tajima, D. Bloch, and M. Roth, <i>Solid State Commun.</i> 19 , 525 (1976). | [10] U. K. Rössler, A. N. Bogdanov, and C. Pfleiderer, <i>Nature (London)</i> 442 , 797 (2006). |
| [4] C. Pfleiderer, S. R. Julian, and G. G. Lonzarich, <i>Nature (London)</i> 414 , 427 (2001). | [11] I. Fischer, N. Shah, and A. Rosch, <i>Phys. Rev. B</i> 77 , 024415 (2008). |
| [5] N. Doiron-Leyraud, I. R. Walker, L. Taillefer, M. J. Steiner, S. R. Julian, and G. G. Lonzarich, <i>Nature</i> 425 , 595 (2003). | [12] S. D. Yi, S. Onoda, N. Nagaosa, and J. H. Han, <i>Phys. Rev. B</i> 80 , 054416 (2009). |
| [6] C. Pfleiderer, D. Reznik, L. Pintschovius, H. v. Löhneysen, M. Garst, and A. Rosch, <i>Nature (London)</i> 427 , 227 (2004). | [13] S. Mühlbauer, B. Binz, F. Jonietz, C. Pfleiderer, A. Rosch, A. Neubauer, R. Georgii, and P. Böni, <i>Science</i> 323 , 915 (2009). |
| [7] C. Pfleiderer, P. Böni, T. Keller, U. K. Rössler, and A. Rosch, <i>Science</i> 316 , 1871 (2007). | [14] B. Lebech, P. Harris, J. Skov Pedersen, K. Mortensen, C. I. Gregory, N. R. Bernhoeft, M. Jermy, and |

- S. A. Brown, *J. Magn. Magn. Mater.* **140-144**, 119 (1995).
- [15] A. Neubauer, C. Pfleiderer, B. Binz, A. Rosch, R. Ritz, P. G. Niklowitz, and P. Böni, *Phys. Rev. Lett.* **102**, 186602 (2009).
- [16] F. P. Mena, D. van der Marel, A. Damascelli, M. Fäth, A. A. Menovsky, and J. A. Mydosh, *Phys. Rev. B* **67**, 241101(R) (2003).
- [17] M. Lee, W. Kang, Y. Onose, Y. Tokura, and N. P. Ong, *Phys. Rev. Lett.* **102**, 186601 (2009).
- [18] A. Yoshimori, *J. Phys. Soc. Jpn.* **14**, 807 (1959).
- [19] T. Moriya, *Phys. Rev.* **120**, 91 (1960).
- [20] I. E. Dzyaloshinsky, *J. Phys. Chem. Solids* **4**, 241 (1958).
- [21] P. Bak and M. H. Jensen, *J. Phys. C: Solid State Phys.* **13**, L881 (1980).
- [22] M. L. Plumer and M. B. Walker, *J. Phys. C: Solid State Phys.* **14**, 4689 (1981).
- [23] M. Kataoka and O. Nakanishi, *J. Phys. Soc. Jpn.* **50**, 3888 (1981).
- [24] M. Plumer, *J. Phys. C: Solid State Phys.* **17**, 4663 (1984).
- [25] J. M. Hopkinson and H.-Y. Kee, *Phys. Rev. B* **79**, 014421 (2009).
- [26] V. A. Chizhikov and V. E. Dmitrienko, *Phys. Rev. B* **85**, 014421 (2012).
- [27] P. Dalmas de Réotier, A. Maisuradze, A. Yaouanc, B. Roessli, A. Amato, D. Andreica, and G. Lapertot, *Phys. Rev. B* **93**, 144419 (2016).
- [28] A. Yaouanc, P. Dalmas de Réotier, B. Roessli, A. Maisuradze, A. Amato, D. Andreica, and G. Lapertot, *Phys. Rev. Res.* **2**, 013029 (2020).
- [29] L. R. Walker and R. E. Walstedt, *Phys. Rev. B* **22**, 3816 (1980).
- [30] K. P. W. Hall, A general model of MnSi-like helical magnets, M.Sc. thesis, Memorial University of Newfoundland, 2020.